Model Predictive Current Control of a Grid Connected Converter With LCL-Filter

Joanie M.C. Geldenhuys*, Hendrik du Toit Mouton†, Arnold Rix‡ and Tobias Geyer§
*†‡Department of Electrical and Electronic Engineering
Stellenbosch University, Private Bag X1, 7602, Matieland, South Africa.
* Email: 16722590@sun.ac.za, Tel: (021) 887-8419, Cel: (+27)78 298 3019
† Email: dtmouton@sun.ac.za
‡ Email: rix@sun.ac.za
§ABB Corporate Research, 5405 Baden-Dattwil, Switzerland
Email: t.geyer@ieee.org

***Abstract*—A method to control the output current of a three-phase grid-tied inverter is presented. An LCL-filter is used to reduce the current distortion injected into the grid. The objective is to minimise current distortion and switching frequency to reduce losses. The control approach is based on finite control set model predictive control with sphere decoding to make the problem computationally tractable for long horizons. A mathematical model was derived that extends on previous work by incorporating the effect of a grid-voltage to the system. The control strategy was evaluated through simulation. The results indicate that this control strategy can achieve the objectives for its application mentioned in the paper.**

***Index Terms*—finite control set model predictive control, long horizons, LCL-filter, grid-connected inverter, sphere decoding, current control.**

I. Introduction

Direct model predictive control (MPC) with reference tracking can be applied to maintain acceptable distortion levels and reduce losses by lowering the switching frequency, which is important in high-power converters [1], [2]. Due to previous limitations of real time processing power, MPC has only recently gained popularity in power electronic applications. MPC performed over long horizons provide solution sequences that perform better in the frequency domain than with a horizon length of one [3] and are close to optimal pulse patterns [4]. In this paper inner-loop current control is performed for a three-phase grid-tied converter using finite control set model predictive control (FCS MPC) over long horizons with sphere decoding. Sphere decoding is implemented to relieve the computational burden of using long horizons by performing a more efficient search process [5], [6]. A mathematical model is derived that extends on theory in [6] and [7] by incorporating the effect of a grid-voltage to the system. The control strategy is evaluated by means of simulation.

The topology of the system is illustrated in Fig. 1. The inverter receives DC power from a renewable source. After the inverter an LCL-filter is added to filter out the harmonics resulting from the converter before the power is supplied to the grid [8]. The filter setup is shown in Fig. 2. LCL-filters have high attenuation abilities compared to series inductor filters and are therefore a good consideration for grid-connected systems [9], [10]. The output current from the inverter i_1, the grid-side current i_2 and the capacitor voltage v_c will be controlled with FCS MPC. The switch state u in each phase-leg can assume one of the two possible switch states in the finite control set $u_a,\ u_b,\ u_c \in \{-1, 1\}$ at each time instance k.

978-1-5090-1815-4/16/$31.00

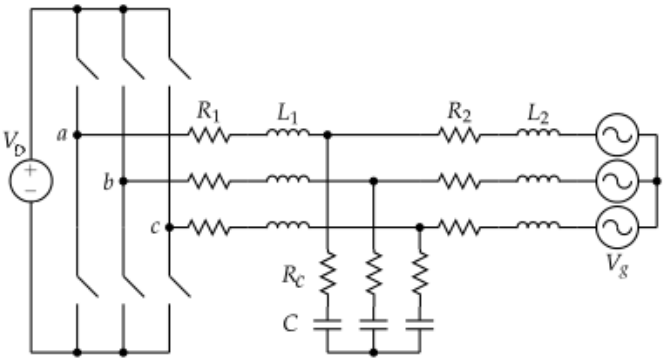

Figure 1: Three-phase grid-connected converter with LCL-filter.

II. System Modelling

The system model in Fig. 1 and 2 is implemented mathematically into a MATLAB-based simulation to evaluate the strategy.

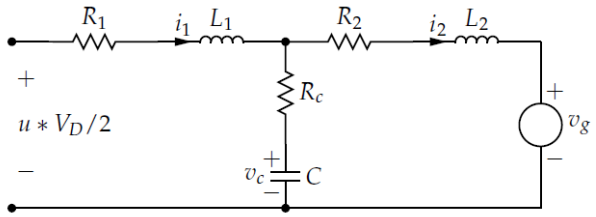

Figure 2: Per-phase model of the LCL-filter.

A. $\alpha\beta$ Reference frame

Three-phase quantities can be transformed from the abc reference frame $\boldsymbol{\xi}_{abc} = [\xi_a \ \xi_b \ \xi_c]^T$ to the stationary orthogonal $\alpha\beta$ reference frame $\boldsymbol{\xi}_{\alpha\beta} = [\xi_\alpha \ \xi_\beta]^T$ by using the transformation in (1) where $\boldsymbol{K}_{\alpha\beta}$ is the transformation matrix.

$$\boldsymbol{\xi}_{\alpha\beta} = \boldsymbol{K}_{\alpha\beta}\boldsymbol{\xi}_{abc} \tag{1}$$

$$\boldsymbol{K}_{\alpha\beta} = \frac{2}{3}\begin{bmatrix} 1 & -\frac{1}{2} & -\frac{1}{2} \\ 0 & \frac{\sqrt{3}}{2} & -\frac{\sqrt{3}}{2} \end{bmatrix} \tag{2}$$

B. Controller model

The continuous-time state-space model is given in equation (3) and (4). The state-variable $\boldsymbol{x} = [\boldsymbol{i}_1 \ \boldsymbol{i}_2 \ \boldsymbol{v}_c]^T$ contains the input-current, output-current and capacitor-voltage vectors in $\alpha\beta$ coordinates, for example $\boldsymbol{i}_2 = [i_{2_\alpha} \ i_{2_\beta}]^T$. The switch states are represented by $\boldsymbol{u} = [u_a \ u_b \ u_c]^T$ and the grid-voltage by $\boldsymbol{v_g} = [v_{g_a} \ v_{g_b} \ v_{g_c}]^T$ which leads to an additional matrix, $\boldsymbol{P}$, to incorporate the effect of the grid in the model. In (4) the state variables that need to be controlled are selected and assigned a constant weighting.

$$\frac{d\boldsymbol{x}(t)}{dt} = \boldsymbol{F}\boldsymbol{x}(t) + \boldsymbol{G}\boldsymbol{u}(t) + \boldsymbol{P}\boldsymbol{v_g}(t) \tag{3}$$

$$\boldsymbol{y}(t) = \boldsymbol{C}\boldsymbol{x}(t) \tag{4}$$

where

$$\boldsymbol{F} = \begin{bmatrix} \frac{R_c+R_1}{-L_1} & 0 & \frac{R_c}{L_1} & 0 & \frac{1}{-L_1} & 0 \\ 0 & \frac{R_c+R_1}{-L_1} & 0 & \frac{R_c}{L_1} & 0 & \frac{1}{-L_1} \\ \frac{R_c}{L_2} & 0 & \frac{R_c+R_2}{-L_2} & 0 & \frac{1}{L_2} & 0 \\ 0 & \frac{R_c}{L_2} & 0 & \frac{R_c+R_2}{-L_2} & 0 & \frac{1}{L_2} \\ \frac{1}{C} & 0 & \frac{1}{-C} & 0 & 0 & 0 \\ 0 & \frac{1}{C} & 0 & \frac{1}{-C} & 0 & 0 \end{bmatrix}$$

$$\boldsymbol{G} = \begin{bmatrix} \frac{V_D}{2L_1} & 0 & 0 & 0 & 0 & 0 \\ 0 & \frac{V_D}{2L_1} & 0 & 0 & 0 & 0 \end{bmatrix}^T \boldsymbol{K}_{\alpha\beta}$$

$$\boldsymbol{P} = \begin{bmatrix} 0 & 0 & \frac{1}{-L_2} & 0 & 0 & 0 \\ 0 & 0 & 0 & \frac{1}{-L_2} & 0 & 0 \end{bmatrix}^T \boldsymbol{K}_{\alpha\beta}$$

$$\boldsymbol{C} = \begin{bmatrix} k_1 & 0 & 0 & 0 & 0 & 0 \\ 0 & k_1 & 0 & 0 & 0 & 0 \\ 0 & 0 & k_2 & 0 & 0 & 0 \\ 0 & 0 & 0 & k_2 & 0 & 0 \\ 0 & 0 & 0 & 0 & k_3 & 0 \\ 0 & 0 & 0 & 0 & 0 & k_3 \end{bmatrix}$$

Exact discretization is done by using (5) - (7) to convert the continuous-time model to a discrete-time model as in (8) and (9). Time is divided into fixed sampling intervals of length T_s and k denotes the current position in time. At each time instance k each phase leg of the system only assumes one of two possible switch states contained in the finite control set $u_a,\ u_b,\ u_c \in \{-1, 1\}$. The model is evaluated at each time instant k to determine the state $\boldsymbol{x}$ at the next time-step $k+1$ as a result of the chosen switch state.

$$\boldsymbol{A} = e^{\boldsymbol{F}T_s} \tag{5}$$

$$\boldsymbol{B} = -\boldsymbol{F}^{-1}(\mathbf{I} - \boldsymbol{A})\boldsymbol{G} \tag{6}$$

$$\boldsymbol{T} = -\boldsymbol{F}^{-1}(\mathbf{I} - \boldsymbol{A})\boldsymbol{P} \tag{7}$$

$$\boldsymbol{x}(k+1) = \boldsymbol{A}\boldsymbol{x}(k) + \boldsymbol{B}\boldsymbol{u}(k) + \boldsymbol{T}\boldsymbol{v_g}(k) \tag{8}$$

$$\boldsymbol{y}(k) = \boldsymbol{C}\boldsymbol{x}(k) \tag{9}$$

C. Model predictive control

The discrete-time state-space model is used to predict the outcome for each possible switch state input $\boldsymbol{u}(k)$. These outcomes are evaluated with the cost function in (10) comprising of two control objectives. The first part of (10) implements the objective to minimise the tracking error $\boldsymbol{y}_e$ between the predicted values of the controlled variables $\boldsymbol{y}$ and their references $\boldsymbol{y}^*$, which is obtained by calculating the steady-state phasor values. The second part represents the objective to lower switching losses by minimising the switching frequency. A weighting factor λ_u is applied to control the trade-off between these two control objectives. The length of the prediction horizon N represents the finite amount of time steps into the future over which the outcomes are evaluated by the cost function [6].

$$J = \sum_{l=k}^{k+N-1} ||\boldsymbol{y}_e(l+1)||_2^2 + \lambda_u \, ||\Delta\boldsymbol{u}(l)||_2^2 \tag{10}$$

$$\boldsymbol{y}_e(k+1) = \boldsymbol{y}^*(k+1) - \boldsymbol{y}(k+1) \tag{11}$$

$$\Delta\boldsymbol{u}(k) = \boldsymbol{u}(k) - \boldsymbol{u}(k-1) \tag{12}$$

By successively applying (8) to itself (13) is derived which is then substituted into (9) to give (14):

$$\begin{aligned} \boldsymbol{x}(k+m) &= \boldsymbol{A}^m\boldsymbol{x}(k) + \sum_{l=0}^{m-1} \boldsymbol{A}^{m-1-l}\boldsymbol{B}\boldsymbol{u}(k+l) \\ &\quad + \sum_{l=0}^{m-1} \boldsymbol{A}^{m-1-l}\boldsymbol{T}\boldsymbol{v_g}(k+l) \end{aligned} \tag{13}$$

$$\begin{aligned} \boldsymbol{y}(k+m) &= \boldsymbol{C}\boldsymbol{x}(k+m) \\ &= \boldsymbol{C}\boldsymbol{A}^m\boldsymbol{x}(k) + \sum_{l=0}^{m-1} \boldsymbol{C}\boldsymbol{A}^{m-1-l}\boldsymbol{B}\boldsymbol{u}(k+l) \\ &\quad + \sum_{l=0}^{m-1} \boldsymbol{C}\boldsymbol{A}^{m-1-l}\boldsymbol{T}\boldsymbol{v_g}(k+l) \end{aligned} \tag{14}$$

for $m = 0, \ldots, N-1$.

The output current (16) is given as the matrix notation of (14) where $\boldsymbol{\Psi}\boldsymbol{V_g}(k)$ is added to the equation from [6]:

$$\boldsymbol{Y}(k) = \begin{bmatrix} \boldsymbol{y}^T(k+1) \ \ldots \ \boldsymbol{y}^T(k+N) \end{bmatrix}^T \tag{15}$$

$$\boldsymbol{Y}(k) = \boldsymbol{\Gamma}\boldsymbol{x}(k) + \boldsymbol{\Upsilon}\boldsymbol{U}(k) + \boldsymbol{\Psi}\boldsymbol{V_g}(k) \tag{16}$$

where

$$\boldsymbol{\Gamma} = \begin{bmatrix} \boldsymbol{CA} & \boldsymbol{CA}^2 & \boldsymbol{CA}^3 & \dots & \boldsymbol{CA}^N \end{bmatrix}^T$$

$$\boldsymbol{\Upsilon} = \begin{bmatrix} \boldsymbol{CB} & \boldsymbol{0} & \cdots & \boldsymbol{0} \\ \boldsymbol{CAB} & \boldsymbol{CB} & \cdots & \boldsymbol{0} \\ \vdots & \vdots & & \vdots \\ \boldsymbol{CA}^{N-1}\boldsymbol{B} & \boldsymbol{CA}^{N-2}\boldsymbol{B} & \cdots & \boldsymbol{CB} \end{bmatrix}$$

$$\boldsymbol{\Psi} = \begin{bmatrix} \boldsymbol{CT} & \boldsymbol{0} & \cdots & \boldsymbol{0} \\ \boldsymbol{CAT} & \boldsymbol{CT} & \cdots & \boldsymbol{0} \\ \vdots & \vdots & & \vdots \\ \boldsymbol{CA}^{N-1}\boldsymbol{T} & \boldsymbol{CA}^{N-2}\boldsymbol{T} & \cdots & \boldsymbol{CT} \end{bmatrix}$$

The cost function (10) is then rewritten in the following form:

$$\begin{aligned} J &= \|\boldsymbol{\Gamma x}(k) + \boldsymbol{\Upsilon U}(k) + \boldsymbol{\Psi V_g}(k) - \boldsymbol{Y}^\star(k)\|_2^2 \\ &\quad +\lambda_u \|\boldsymbol{SU}(k) - \boldsymbol{Eu}(k-1)\|_2^2 \\ &= \|\boldsymbol{\Gamma x}(k) - \boldsymbol{Y}^\star(k)\|_2^2 + \|\boldsymbol{\Psi V_g}(k)\|_2^2 \\ &\quad +\lambda_u \|\boldsymbol{Eu}(k-1)\|_2^2 + 2\left[\boldsymbol{\Gamma x}(k) - \boldsymbol{Y}^\star(k)\right]^T \boldsymbol{\Psi V_g}(k) \\ &\quad +2\left[\boldsymbol{\Gamma x}(k) - \boldsymbol{Y}^\star(k)\right]^T \boldsymbol{\Upsilon U}(k) + 2\left[\boldsymbol{\Upsilon U}(k)\right]^T \boldsymbol{\Psi V_g}(k) \\ &\quad -2\lambda_u \left\{\left[\boldsymbol{Eu}(k-1)\right]^T \boldsymbol{SU}(k)\right\} \\ &\quad +\boldsymbol{U}(k)^T \left\{\boldsymbol{\Upsilon}^T\boldsymbol{\Upsilon} + \lambda_u \boldsymbol{S}^T\boldsymbol{S}\right\} \boldsymbol{U}(k) \end{aligned} \tag{17}$$

where $\boldsymbol{S}$ and $\boldsymbol{E}$ consist of zero and identity matrices. More detail can be obtained in [6]. The sixth term in (17), resulting in a 1-by-1 matrix, can be rewritten as follows:

$$\begin{aligned} 2\left[\boldsymbol{\Upsilon U}(k)\right]^T \boldsymbol{\Psi V_g}(k) &= 2\left\{\left[\boldsymbol{\Upsilon U}(k)\right]^T \left[\boldsymbol{\Psi V_g}(k)\right]\right\}^T \\ &= 2\left[\boldsymbol{\Psi V_g}(k)\right]^T \left[\boldsymbol{\Upsilon U}(k)\right] \\ &= 2\boldsymbol{V_g}^T(k)\boldsymbol{\Psi}^T\boldsymbol{\Upsilon U}(k) \end{aligned}$$

The cost function can be written in the more compact form:

$$J = \theta(k) + 2\boldsymbol{\Theta}^T(k)\boldsymbol{U}(k) + \|\boldsymbol{U}(k)\|_{\boldsymbol{Q}}^2 \tag{18}$$

where

$$\begin{aligned} \theta(k) &= \|\boldsymbol{\Gamma x}(k) - \boldsymbol{Y}^\star(k)\|_2^2 + \|\boldsymbol{\Psi V_g}(k)\|_2^2 \\ &\quad +\lambda_u \|\boldsymbol{Eu}(k-1)\|_2^2 \\ &\quad +2\left[\boldsymbol{\Gamma x}(k) - \boldsymbol{Y}^\star(k)\right]^T \boldsymbol{\Psi V_g}(k) \end{aligned} \tag{19}$$

$$\begin{aligned} \boldsymbol{\Theta}(k) &= \{\left[\boldsymbol{\Gamma x}(k) - \boldsymbol{Y}^\star(k)\right]^T \boldsymbol{\Upsilon} + \boldsymbol{V_g}^T(k)\boldsymbol{\Psi}^T\boldsymbol{\Upsilon} \\ &\quad -\lambda_u \left[\boldsymbol{Eu}(k-1)\right]^T \boldsymbol{S}\}^T \end{aligned} \tag{20}$$

$$\boldsymbol{Q} = \boldsymbol{\Upsilon}^T\boldsymbol{\Upsilon} + \lambda_u \boldsymbol{S}^T\boldsymbol{S} \tag{21}$$

In (19) to (21), $\theta(k)$ and $\boldsymbol{\Theta}(k)$ are changed by the influence of $\boldsymbol{V_g}$ while $\boldsymbol{Q}$ remains the same as in [6]. The optimal switching sequence is identified by searching for the sequence that results in the minimum cost, J, in (10). In (22) this problem is reformulated into an integer least-squares problem in vector form. The unconstrained optimum $\boldsymbol{U}_{unc}$ is the optimal solution sequence obtained by eliminating the integer constraints of the switch state $\boldsymbol{u}$ [6]. Due to a changed $\boldsymbol{\Theta}(k)$, $\boldsymbol{U}_{unc}$ differs from that in [6] due to the influence of the grid. The transformation matrix $\boldsymbol{H}$ is a lower triangular matrix obtained in (24) by taking the Cholesky decomposition of Q^{-1} and will remain the same as $\boldsymbol{Q}$ remains unchanged with regards to [6]. To illustrate its influence, an example is presented in Fig. 3 of a three-phase system over a horizon of N = 1. Each axis in the orthogonal coordinate system represents the switch state of one phase-leg. The dashed line cube represents the orthogonal solution space and the points on its vertices all candidate sequences. The orthogonal coordinate system is transformed by multiplication with the transformation matrix $\boldsymbol{H}$ and delivers a scaled and skewed solution space, indicated by the small solid line cube in Fig. 3. An exhaustive search has to be performed by evaluating every point $\boldsymbol{HU}$ with (22) to identify the solution with the shortest euclidean distance from the transformed unconstrained solution $\bar{\boldsymbol{U}}_{unc}$. The amount of candidate solutions can be expressed as 2^{3N}. This approach is only feasible for short horizons for as N increases the amount of candidate solutions increase exponentially. For long horizons a sphere decoding algorithm can optimize the search process.

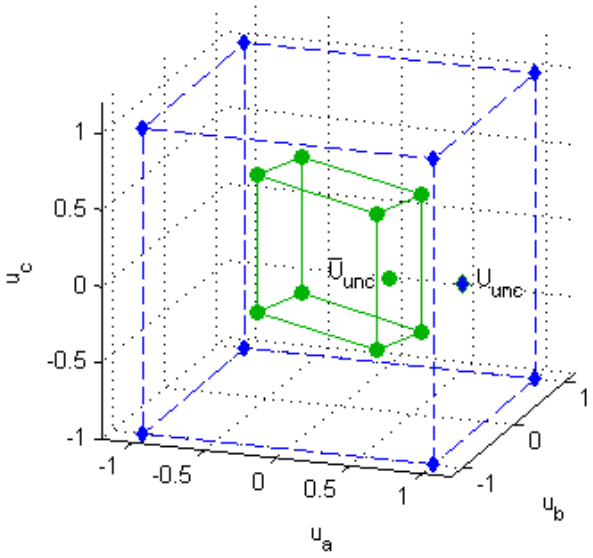

Figure 3: Visualization of the optimization problem in an orthogonal coordinate system (dashed line) and how the transformed problem (solid line) compares for a three-phase system with a horizon of $N = 1$.

$$\boldsymbol{U}_{opt}(k) = \arg\min_{\boldsymbol{U}(k)} \left\|\boldsymbol{HU}(k) - \bar{\boldsymbol{U}}_{unc}(k)\right\|_2^2 \tag{22}$$

where

$$\boldsymbol{U}_{unc}(k) = -\boldsymbol{Q}^{-1}\boldsymbol{\Theta}(k) \tag{23}$$

$$\boldsymbol{H}^T\boldsymbol{H} = \boldsymbol{Q} \tag{24}$$

$$\bar{\boldsymbol{U}}_{unc}(k) = \boldsymbol{HU}_{unc}(k) \tag{25}$$

D. Sphere decoding

The aim of sphere decoding is to exclude as many suboptimal solutions from the search as possible by only evaluating solution points within the radius of a sphere, ρ in (26),

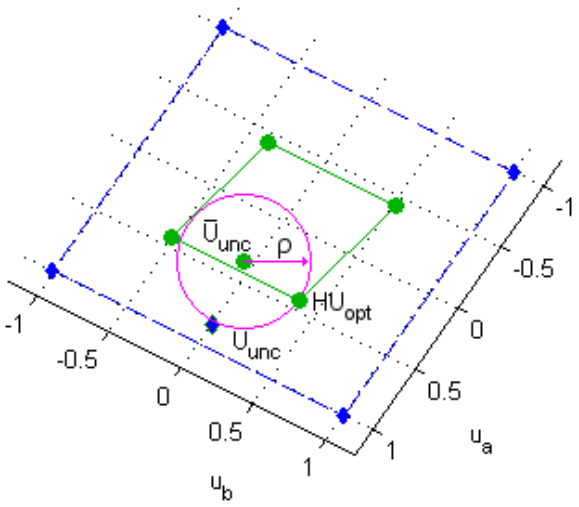

Figure 4: Top view of Fig. 3 showing the ab-plane to gain perspective on the sphere and the points which lay closest to its centre.

centred around the transformed unconstrained optimum $\bar{\boldsymbol{U}}_{unc}$. It is important to choose the initial radius in such a way that it is small enough to eliminate as many candidate switching sequences as possible, yet large enough to avoid having an empty solution due to all solutions falling outside of the sphere. In (27) the initial radius is calculated with an initial estimate $\boldsymbol{U}_{ini}(k)$ of a possible optimum solution. The initial solution estimate is determined by component-wise rounding of the unconstrained solution in (23) to the nearest finite control set values of 1 or -1. This is known as the Babai estimate [5].

$$\rho(k) \geq \left\|\bar{\boldsymbol{U}}_{unc}(k) - \boldsymbol{H}\boldsymbol{U}(k)\right\|_2 \quad (26)$$

$$\rho_{ini}(k) = \left\|\bar{\boldsymbol{U}}_{unc}(k) - \boldsymbol{H}\boldsymbol{U}_{ini}(k)\right\|_2 \quad (27)$$

In Fig. 4, viewing the solution space in Fig. 3 from above, an example is given of how the sphere is applied. The unconstrained optimum $\boldsymbol{U}_{unc}$ of the orthogonal solution space is an equal distance away from two possible solution points $[1\ 1\ 1]^T$ and $[1\ -1\ 1]^T$. The optimal solution cannot be declared before the transformation by applying $\boldsymbol{H}$ has been performed as in (22). In the transformed solution space it is observed that the one solution point falls outside of the sphere before the other, therefore exposing the true optimal solution $\boldsymbol{U}_{opt}$.

III. Results

The mathematical model of the current control strategy was evaluated by implementing it in a MATLAB-based simulation. The weightings in the $\boldsymbol{C}$ matrix were assigned the values $k_1 = k_2 = 1$ and $k_3 = 0.1$. The frequency of the grid voltage and the reference current is set to 50 Hz. The dc-link voltage V_D is constant at 1000 V and the amplitude

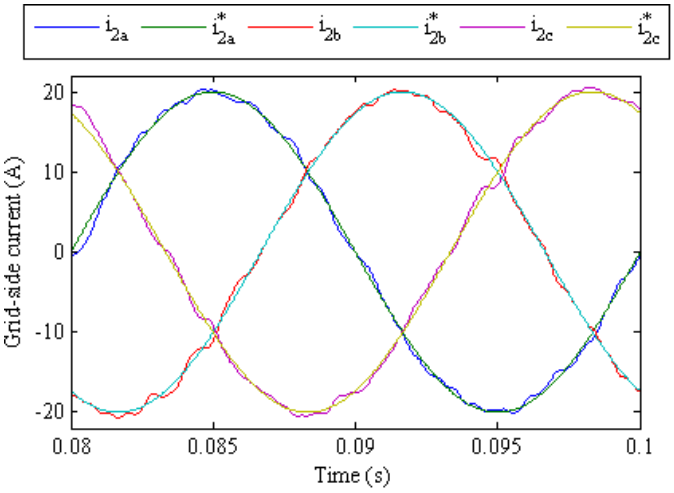

Figure 5: Steady-state three-phase output current and references.

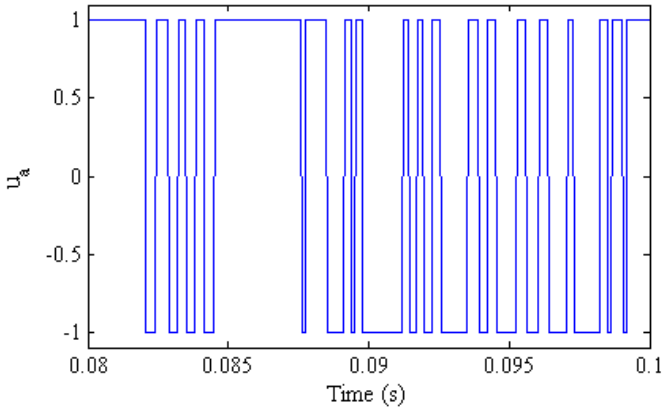

Figure 6: Switching sequence of the a-phase.

of the reference current is 20 A. The grid voltage V_g has an amplitude of $230\sqrt{2}$ V. The parameters for the LCL-filter are L_1 = 20 mH, L_2 = 1.6 mH, C = 65.25 μF, $R_1 = R_2 = R_c$ = 0.1 Ω. The weighting factor is set as λ_u = 6 and the sampling interval T_s = 40 μs. A horizon length of N = 14 is applied. The steady-state three-phase output currents of $\boldsymbol{i}_2$ and their references are shown in Fig. 5 and Fig. 6 shows the switching sequence applied for the a-phase. A more detailed view of the a-phase grid-side current is given in Fig. 7. The behaviour of the converter-side inductor current and the capacitor voltage is shown in Fig. 8 and Fig. 9. From the spectrum of i_{2a} in Fig. 10 it is observed that the current-tracking error of the fundamental 50 Hz component is 0.18%. The total harmonic distortion (THD) of the grid-side current is 4.03% and the switching frequency is f_s = 0.82 kHz. The response of the system to a step in amplitude of the grid-side reference current is observed in Fig. 11, 12 and 13.

IV. Conclusion

The paper presented a strategy to control the output current of a three-phase grid-tied converter with LCL-filter through

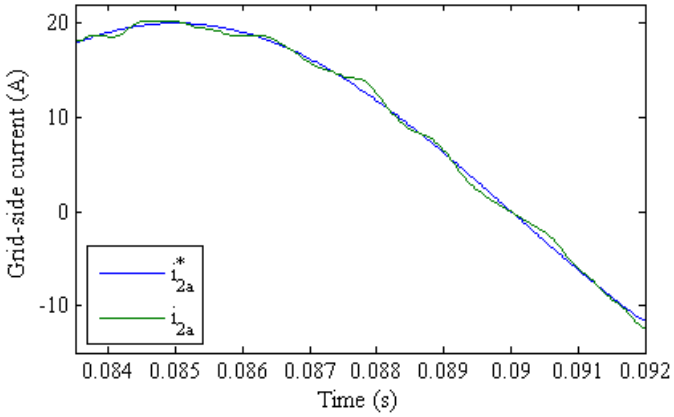

Figure 7: Output current and current reference of the a-phase during steady-state.

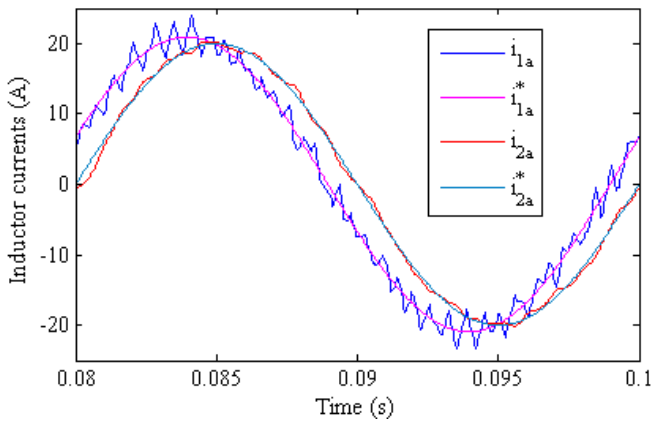

Figure 8: Inductor currents and references in the a-phase during steady-state.

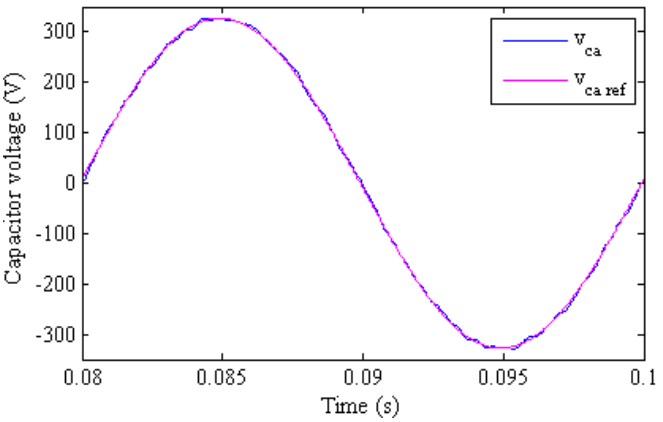

Figure 9: Capacitor voltage and its reference in the a-phase during steady-state.

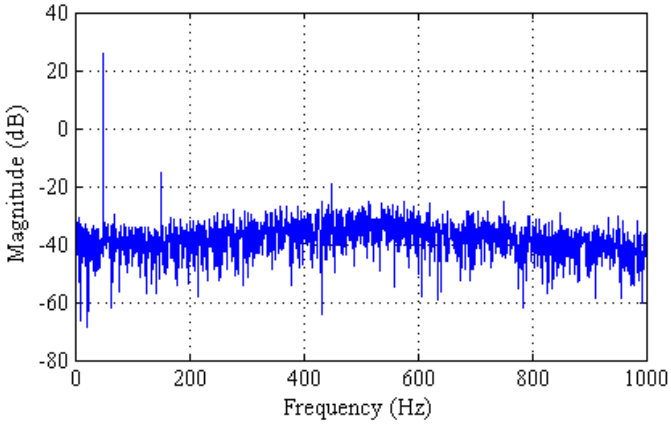

Figure 10: Output current spectrum of the a-phase.

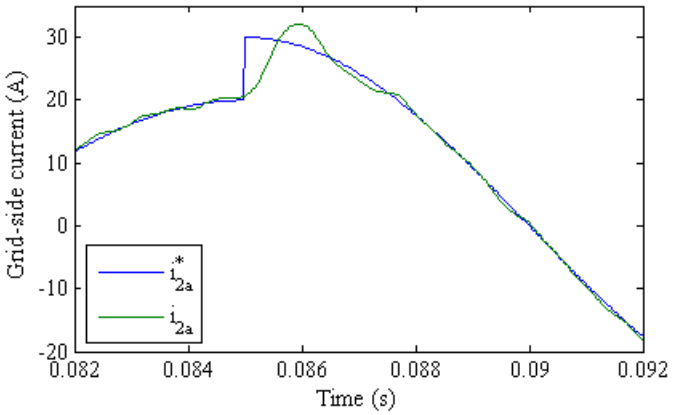

Figure 11: Response to an amplitude step in the sinusoidal current reference.

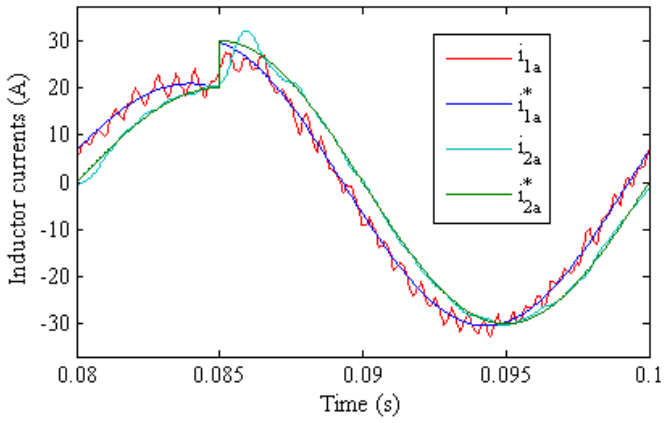

Figure 12: Response of inductor currents to a step in the references.

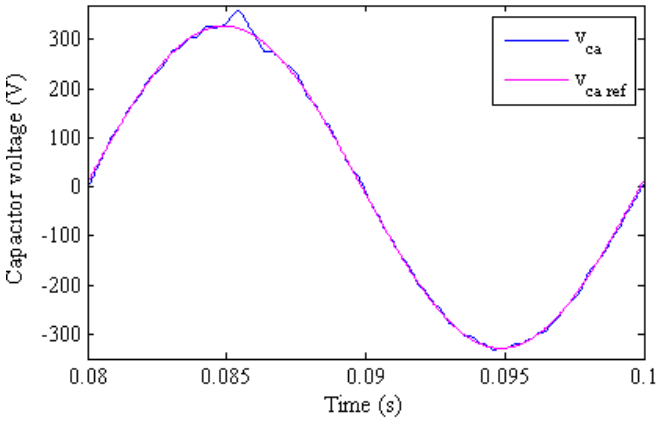

Figure 13: Response of the capacitor voltage to a step in the a-phase.

model predictive control over long horizons with sphere decoding. The control objectives were to minimise current-tracking error and reduce losses by minimising the switching frequency. The strategy was evaluated through simulation with a horizon length of fourteen. It is demonstrated that the control scheme delivered satisfactory results such as a tracking error of 0.18%, a current THD of 4.03% and a switching frequency of 0.82 kHz.

ACKNOWLEDGMENT

This research was supported by the Scatec Solar Bursary.

REFERENCES

[1] J. Scoltock, T. Geyer, and U. Madawala, "Model predictive direct current control for a grid-connected converter: LCL-filter versus L-filter," in *Industrial Technology (ICIT), 2013 IEEE International Conference on*, Feb 2013, pp. 576–581.

[2] J. Scoltock, T. Geyer, and U. Madawala, "Model predictive direct power control for a grid-connected converter with an LCL-filter," in *Industrial Technology (ICIT), 2013 IEEE International Conference on*, Feb 2013, pp. 588–593.

[3] T. Geyer and D. E. Quevedo, "Performance of multistep finite control set model predictive control for power electronics," *IEEE Transactions on Power Electronics*, vol. 30, no. 3, pp. 1633–1644, March 2015.

[4] T. Geyer, N. Oikonomou, G. Papafotiou, and F. D. Kieferndorf, "Model predictive pulse pattern control," *IEEE Transactions on Industry Applications*, vol. 48, no. 2, pp. 663–676, March 2012.

[5] P. Karamanakos, T. Geyer, and R. Kennel, "Reformulation of the long-horizon direct model predictive control problem to reduce the computational effort," in *2014 IEEE Energy Conversion Congress and Exposition (ECCE)*, Sept 2014, pp. 3512–3519.

[6] T. Geyer and D. E. Quevedo, "Multistep finite control set model predictive control for power electronics," *IEEE Transactions on Power Electronics*, vol. 29, no. 12, pp. 6836–6846, Dec 2014.

[7] T. Geyer, P. Karamanakos, and R. Kennel, "On the benefit of long-horizon direct model predictive control for drives with LC filters," in *2014 IEEE Energy Conversion Congress and Exposition (ECCE)*, Sept 2014, pp. 3520–3527.

[8] A. Reznik, M. G. Simões, A. Al-Durra, and S. M. Muyeen, "LCL filter design and performance analysis for grid-interconnected systems," *IEEE Transactions on Industry Applications*, vol. 50, no. 2, pp. 1225–1232, March 2014.

[9] J. Scoltock, T. Geyer, and U. K. Madawala, "A model predictive direct current control strategy with predictive references for MV grid-connected converters with LCL-filters," *IEEE Transactions on Power Electronics*, vol. 30, no. 10, pp. 5926–5937, Oct 2015.

[10] H. Miranda, R. Teodorescu, P. Rodriguez, and L. Helle, "Model predictive current control for high-power grid-connected converters with output LCL filter," in *Industrial Electronics, 2009. IECON '09. 35th Annual Conference of IEEE*, Nov 2009, pp. 633–638.